J. Chem. Sci. (2020) 132:101
https://doi.org/10.1007/s12039-020-01806-0

REGULAR ARTICLE

Preparation of a hollow cube $NiCo_2S_4$ and its application in supercapacitor

XIAOSHAN LI[a], YOU FU[a], HANG MA[a], XILONG LIU[b], LINA LI[a], JIAN MA[a], CONGJIE LIANG[a], MENG JIN[a], YINGJIE HUA[a,*] and CHONGTAI WANG[a,*]

[a]Key Laboratory of Electrochemical Energy Storage and Energy Conversion of Hainan Province, School of Chemistry and Chemical Engineering, Hainan Normal University, Haikou South Longkun Rd., Haikou 571158, People's Republic of China

[b]Chemical college of Jilin University, Changchun 130000, People's Republic of China

E-mail: 521000hua282@sina.com; oehy2014@163.com

MS received 6 February 2020; revised 15 April 2020; accepted 15 April 2020

Abstract. Here reports a hollow cube $NiCo_2S_4$ nanomaterial, which was prepared via facile hydroxylation and sulfuration steps using the self-prepared ZIF-67 as a precursor. This kind of $NiCo_2S_4$ as an electrode material for supercapacitor presents a specific capacitance high up to 1350 F g^{-1} at 1 A g^{-1} due to the contribution of pseudocapacitance. Particularly, the hybrid supercapacitor PC//$NiCo_2S_4$, assembled using the $NiCo_2S_4$ as the positive electrode material and the PC as the negative electrode material, delivers a high energy density of 33 Wh kg^{-1} at the power density of 800 W kg^{-1}. Meanwhile, it presents a good cyclic stability with 67% capacitance retention after 10,000 cycles of charge–discharge at the current density of 5 A g^{-1}. However, the rate capability is not good enough because of the polarization effect of $NiCo_2S_4$ as a battery-type electrode material. Therefore, this research provides a reference for enhancing capacitance performance of an electrode material. For instance, reversibility in redox reaction and stability in structure are more important than the capacity in many cases.

Keywords. Electrochemistry; capacitance; energy density; ZIF-67; nanomaterial.

1. Introduction

With the development of renewable energy such as solar, wind and tidal power, large-scale energy storage devices are urgently needed. At the same time, power station peak regulation, urban transport vehicles and portable electronic equipment also need safe, stable, long life, high power and large capacity's energy storage devices and power supply. Therefore, relevant research has become a research hotspot in the world[1,2]. Thereinto, supercapacitors have received a lot of attention due to the advantages such as rapid charging, long cycle life, high power density and safety[3–8]. Supercapacitors store electrical energy in two types: double-layer capacitance and pseudocapacitance. The former stores electrical energy by forming double layers through adsorbing oppositely charged ions from electrolyte solution at the interface of electrode, while the latter stores electrical energy through a rapid redox reaction at the surface of electrode. The specific capacity of pseudocapacitance is usually much larger than that of the double layer capacitance[9]. Transition metal oxides or hydroxides such as RuO_2[10], MnO_2[3], Co_3O_4[11] and $Ni(OH)_2$[12] are typical pseudocapacitive materials, which have widely been researched as hotspot materials due to the merits of high theoretical specific capacitance, environmental friendliness and low cost[13–16]. However, these pseudocapacitive materials usually present a poor electrical conductivity, thus making their capacitance performance decrease greatly. Therefore, in order to overcome this drawback, bimetallic oxides have been exploited as electrode materials for supercapacitors. Among them, ternary nickel-cobalt oxide $NiCo_2O_4$ has been widely studied due to its higher electrical

*For correspondence

Electronic supplementary material: The online version of this article (https://doi.org/10.1007/s12039-020-01806-0) contains supplementary material, which is available to authorized users.

Published online: 09 August 2020

conductivity and multiple redox states compared to binary transition metal oxides[3,17, 18]. Introduction of the bivalent nickel or the trivalent cobalt resulted really in improvement of the material's capacitance performance because of the synergistic effect between Ni(II) and Co(III)[18].

Recently, however, it was found that using sulfides instead of oxides could lead to better performance. For example, vulcanization of $NiCo_2O_4$ into $NiCo_2S_4$ could improve conductivity by two orders of magnitude[19–21]. The specific capacitance was also enhanced obviously, e.g., increased from 1588 F g^{-1} to 2044 F g^{-1} at the current density of 1 A g^{-1}[17]. At present, some common methods for experimentally preparing ternary transition metal sulfide include co-precipitation, sol-gel, hydrothermal process, electrospinning, electrodeposition, self-template, etc.[3,8,22–24]. Utilization of these methods can prepare various ternary transition metal sulfide materials with different morphologies. As well known, different morphologies will bring remarkable influence on the performance of materials. It has been found that metal–organic frameworks (MOFs) have some advantages such as high surface areas, remarkable porosity, enormous structure diversity, etc.[3] Therefore, utilizing MOFs as sacrificial templates can fabricate desired materials with a specified structure and morphology. According to this strategy, a novel hollow cube $NiCo_2S_4$ nano-material was prepared by a simple stirring and high temperature reflux process using ZIF-67 as a precursor and the sodium sulfide as sulfur source in this paper. The as-synthesized hollow cube $NiCo_2S_4$ is expected to have better capacitance performance as an electrode material for supercapacitors.

2. Experimental

2.1 *Chemicals*

2-Methylimidazole ($C_4H_6N_2$), hexadecyl trimethyl ammonium bromide (CTAB), cobalt nitrate hexahydrate [$Co(NO_3)_2{\cdot}6H_2O$] and nickel nitrate hexahydrate [$Ni(NO_3)_2{\cdot}6H_2O$] were purchased from McLean Biochemical Technology Co. Ltd; sodium sulfide nonahydrates ($Na_2S{\cdot}9H_2O$), potassium hydroxide (KOH) and anhydrous ethanol (CH_3CH_2OH) were purchased from Xilong Scientific Co., Ltd.; acetone (CH_3COCH_3) and hydrochloric acid (HCl) were purchased from Tianjin Fuchen chemical reagent factory. All of the reagents were of analytical grade and were used without further purification. Solutions used throughout the testing were prepared with deionized water.

2.2 *Preparation of the hollow cube $NiCo_2S_4$*

After making a little change according to the synthesis method reported by Hu *et al* [25,26], the typical synthesis steps are as follows: 2.724 g 2-methylimidazole, 0.174 g cobalt nitrate hexahydrate and 3 mg CTAB were dissolved into the 46 mL of distilled water, getting purple solution, and then magnetically stirred for 50 min. The resulting ZIF-67 products were collected by centrifugation, washed with anhydrous ethanol several times, and dried in a 60 °C oven. After ultrasonic dissolution of 40 mg ZIF-67 in 15 mL of anhydrous ethanol, the resulting solution was poured into 10 mL of ethanol solution containing 80 mg nickel nitrate hexahydrate, stirred for 50 min to obtain the light purple ZIF-67/Ni-Co layered double hydroxides (LDH) solution, then centrifuged and washed with anhydrous ethanol. The ZIF-67/Ni-Co LDH obtained above was dissolved in 20 mL of anhydrous ethanol; meanwhile, 110 mg of sodium sulfide 9-hydrates was dissolved in 10 mL of 1:1 ethanol solution. The above two solutions were mixed and transferred to reflux at 85 °C for 2 h. The black $NiCo_2S_4$ products were collected by centrifugation, washed several times with anhydrous ethanol and deionized water, and dried for use. The above preparation process is intuitively illustrated in Scheme 1.

2.3 *Preparation of the porous carbon material*

The porous carbon (PC) material used to assemble a hybrid supercapacitor device was prepared by a series of procedures including freeze-drying, carbonization and activation using Bitter tea leaves as precursor. The as-prepared PC has a BET specific surface area of about 2371 m^2g^{-1} and a specific capacitance of about 311 Fg^{-1} at 1 Ag^{-1}.

2.4 *Characterization of the materials*

To characterize the surface morphology and internal microstructure of the as-prepared samples, their SEM and TEM images were recorded using a JEOL JSM-7100F scanning electron microscope (Tokyo, Japan) and a transmission electron microscope (CM10, Philips), respectively; meanwhile, the chemical element and relative element content were analyzed by using the energy dispersive spectroscopy (EDS). The BET specific surface area, pore diameter size and distribution of samples were measured through nitrogen adsorption-desorption isotherms at 77 K using

ASAP 2020 system equipped with an automated surface area and pore size analyzer. The XRD patterns of samples were recorded using a Bruker D8 ADVANCE X-ray diffractometer (Karisruhe, Germany); the radiation source used is Cu-Kα_1 ray with a wavelength of 0.154056 nm; the tube voltage and current are 40 KV and 40 mA, respectively. The chemical element components and their chemical valence states of samples were determined using ESCALAB 250 X-ray photoelectron spectroscope (XPS).

2.5 *Electrochemical measurements*

Before measurement, the $NiCo_2S_4$ electrode was fabricated according to steps as follows: Firstly, the nickel foam was cut into slices with a size of 1 cm × 3 cm, then washed with acetone, diluted hydrochloric acid and ethanol, respectively, and dried under vacuum at 70 °C for use. Secondly, $NiCo_2S_4$, acetylene black and polytetrafluoroethylene (PTFE) were mixed and ground evenly in an agate mortar according to the mass ratio of 7:2:1, then the resulting slurry was rolled into thin sheet on the glass. Finally, a slurry thin slice with a size of 1 cm×1 cm was pressed on the foam nickel prepared above on a tablet press under a pressure of 4 Mpa. The mass loading of the $NiCo_2S_4$ active material is 1.3 mg in the three-electrode system. Whereas in the two-electrode system (button cell), the mass loading of $NiCo_2S_4$ is 1.2 mg, PC is 2.9 mg; the total mass of active materials is 4.1 mg. A filter paper and 2 mol L^{-1} KOH aqueous solution are used as the membrane and the supporting electrolyte, respectively. The digital photo of an assembled button supercapacitor device is provided in in Figure 3S (Supplementary Information). Electrochemical measurements such as cyclic voltammetry (CV), electrochemical impedance spectroscopy (EIS) and galvanostatic charge–discharge (GCD) were conducted on the CHI766D electrochemical workstation (Shanghai Chenhua). A single-chamber electrolytic cell was used with the prepared $NiCo_2S_4$ electrode as working electrode, platinum plate as counter electrode and Hg/HgO electrode as reference electrode. Prior to each measurement, oxygen dissolved in the solution was degassed with nitrogen for 10 min. The cycling stability tests were performed on the TC53 battery test system (NEWARE, China). The 2 mol L^{-1} KOH solution was used as the supporting electrolyte. The specific capacitance of electrode materials was calculated in terms of GCD curves according to equation (1):

$$C_s = \frac{I\Delta t}{m\Delta V} \tag{1}$$

where, I is the electric current value (A); Δt is the discharge time (s); m is the mass of the active substance (g); ΔV is the voltage window (V).

A hybrid supercapacitor (HSC) with a working voltage of 1.6 V was assembled using $NiCo_2S_4$ as positive electrode and the self-prepared porous carbon (PC) as negative electrode. Its energy density and power density were estimated according to equations (2) and (3) :

$$E = \frac{1}{2}CV^2 \tag{2}$$

$$P = \frac{E}{t} \tag{3}$$

Where, C is the capacitance of the device (F g^{-1}); V is the working voltage window of the device (V); t is the discharge time (s).

3. Results and Discussion

3.1 *Characterization of the materials*

The SEM and TEM images characterizing the surface and internal microstructure of the synthesized samples are displayed in Figure 1. It can be seen that the zeolitic imidazolate frameworks (ZIF-67), yielded from the reaction of cobalt ions with 2-methylimidazole under the guidance of the CTAB as template, presents a farctate cubic structure similar to "coffee candy" with a size of about 210 nm (Figure 1a,d). Dissolving ZIF-67 together with nickel nitrate

Scheme 1. Schematic diagram of $NiCo_2S_4$ preparation process.

hexahydrate in absolute ethyl alcohol under magnetic stirring produced ZIF-67/Ni-Co layered double hydroxides (LDH). The resulting ZIF-67/Ni-Co LDH still retained the cube structure of ZIF-67; however, it has become hollowed, and its surface became rough due to the formation of surface hierarchical structure (Figure 1b,e). These variations result from the co-reaction of Ni^{2+} and Co^{2+} with OH^-. The formation of hollow structure may be attributed to a more rapid reaction of OH^- with Co^{2+} owing to the Kirkendall effect[8]. EDS element analyses provide the evidence of cobalt and nickel co-existence (Figure 1S, Supplementary Information). High temperature reflux of ZIF-67/Ni-Co LDH and sodium sulfide in aqueous ethanol yielded the black $NiCo_2S_4$ through the ion-exchange reaction between OH^- and S^{2-}. Alike with the ZIF-67/Ni-Co LDH, the $NiCo_2S_4$ also keeps the hollow cubic structure with the ZIF-67 framework, but the sheet hierarchical structure on the surface is more clear (-Figure 1c,f). EDS element analyses display the existence of S, Co, Ni, proving the sulfuration transformation of ZIF-67/Ni-Co LDH (Figure 1S, Supplementary Information).

X-ray diffraction (XRD) spectra revealed the phase structure and crystallization situation of the synthesized samples. As shown in Figure 2, all of the diffraction peaks for the ZIF-67 sample can be clearly observed and are in agreement with those reported in reference[27]. The typical diffraction peaks appearing at the low angles of 7.24°, 10.27°, 12.64° and 17.94° results from the diffraction of (011), (002), (112) and (222) lattice plane of ZIF-67, respectively[27,28]. Sharp diffraction peaks indicate that ZIF-67 crystals have good crystallinity. After formation of the ZIF-67/Ni-Co LDH, the peaks corresponding to (114) and (223) planes become a little wider except the typical diffraction peaks. This is because parts of the cobalt organic framework complex were transformed into layered double metal hydroxides together with nickel[28,29], which is consistent with the result observed by SEM. The sample obtained through the reaction of ZIF-67/Ni-Co LDH with sodium sulfide shows the weak diffraction peaks of $NiCo_2S_4$ at the 2θ angles of 27.5°, 32.4°, 33.9°, 39.2°, 56.8° and 59.7°, corresponding to the crystal face of (220), (311), (222), (400), (440) and (531), respectively (JCPDS No. 20-0782). This result indicates that the synthesized sample is just the expected $NiCo_2S_4$. Apparently, the poor crystallinity of $NiCo_2S_4$ accounts for the weak diffraction peaks.

XPS tests further provide a chemical composition and valence state information about $NiCo_2S_4$. As shown in Figure 3, Ni, Co and S elements can be observed in the binding energy spectrum in the range from 0 to 1200 eV. The signals of C and O probably result from the residual ZIF-67 and ZIF-67/Ni-Co LDH rather than the atmospheric contamination[24]. In the high resolution spectrum of Ni 2p, the Ni $2p_{3/2}$ and

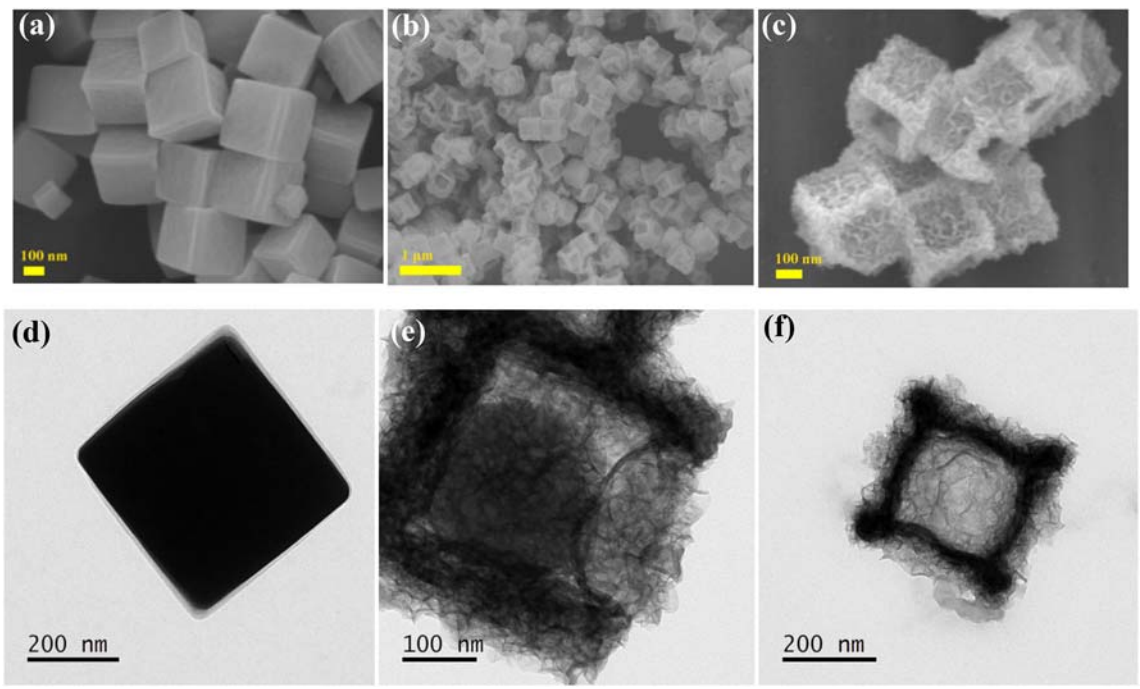

Figure 1. SEM and TEM images of the synthesized samples: (a, d) ZIF-67; (b, e) ZIF-67/Ni-Co-LDH; (c, f) $NiCo_2S_4$.

Ni $2p_{1/2}$ states of Ni^{2+} can be observed at the position of 857.31 eV and 874.96 eV. The shoulder peaks at 862.95 eV and 881.13 eV are the corresponding states of Ni^{3+}. Similarly, the peaks at 782.49 eV and 798.52 eV are assigned to the Co $2p_{1/2}$ and $2p_{3/2}$ states of Co^{3+} in the Co 2p spectrum; the shoulder peaks at 787.46 eV and 804.18 eV are the states of Co^{2+}. Therefore, Cobalt and Nickel are mainly positive trivalent and divalent in $NiCo_2S_4$, respectively. Whereas the Sulfur is negative divalent because the S $2p_{1/2}$ and S $2p_{3/2}$ states of S^{2-} can be observed at 163.49 eV and 168.91 eV in the S 2p spectrum.

Generally, the specific area and the pore size distribution of the electrode material have an important influence on its capacitance performance. Therefore, N_2 adsorption–desorption BET tests for the $NiCo_2S_4$ material were carried out to get these information. The results are illustrated in Figure 4. It can be seen that the N_2 adsorption–desorption isotherm presents a clear hysteresis loop in the range of 0.40–0.99 P/P^0 relative pressure, indicating the existence of mesoporous structure. The pore size distribution mainly focuses on the range of 4–7 nm. The BET specific surface area estimated in terms of the N_2 adsorption-desorption experiment is ca 46 m^2g^{-1}.

3.2 *Electrochemical performance*

The electrochemical performances of the $NiCo_2S_4$ material were measured using a three-electrode system. The results are shown in Figure 5. The cyclic voltammograms in Figure 5a exhibit a pair of redox peaks at the potential of 0.38/0.2 V when the scan rate is 3 mV s^{-1}. Obviously, the peak potential difference between the reduction peak and the oxidation peak is relatively large (about 180 mV); also, both the anodic peak potential and the cathodic one shift remarkably when the scan rate increases from 3 to 30 mVs^{-1}, leading to an increase of peak-to-peak separation. These results demonstrate that $NiCo_2S_4$ has poor redox reversibility, and its Faradaic response is quasi-reversible. Moreover, we note that there is a very small reduction peak appearing at around 0.3V in the cyclic voltammograms. This is caused by residual $Ni(OH)_2$ on the foam nickel matrix due to incomplete clearance. Typically, a pair of current peaks rather than a rectangular shape observed in the cyclic voltammogram indicates that the $NiCo_2S_4$ is a kind of battery-type electrode material, similar to $NiCo_2O_4$[18, 30]. This redox response is due to the redox reaction of the

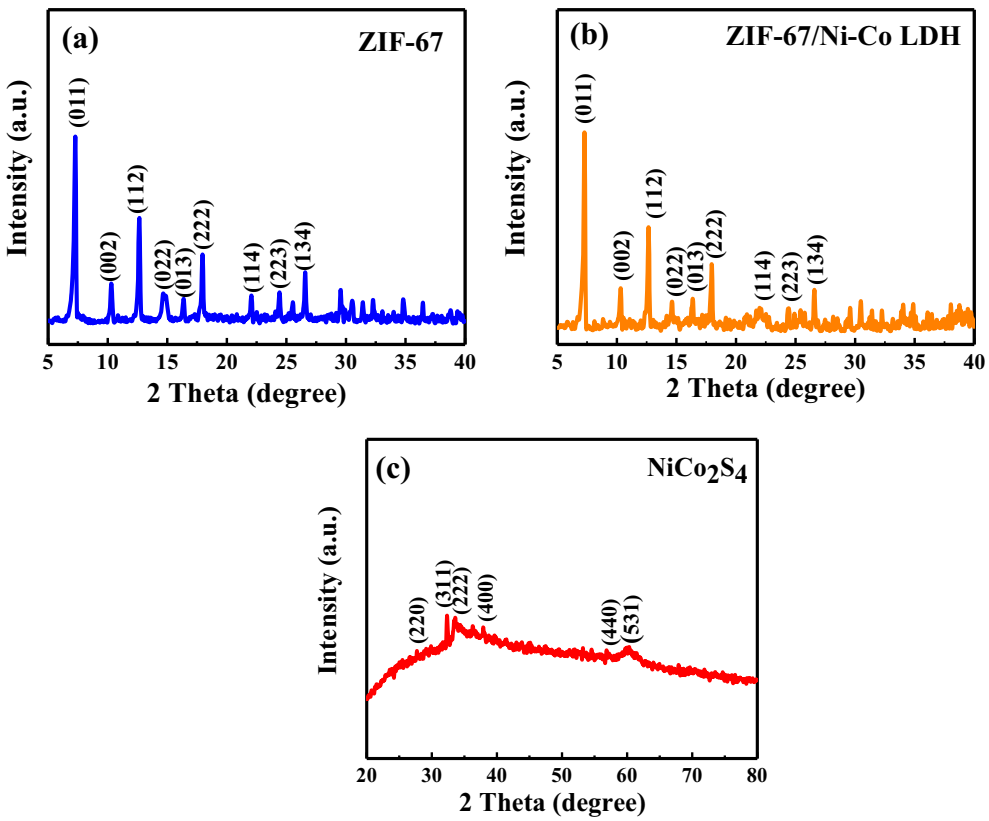

Figure 2. XRD patterns of the synthesized samples: (a) ZIF-67; (b) ZIF-67/Ni-Co LDH; (c) $NiCo_2S_4$.

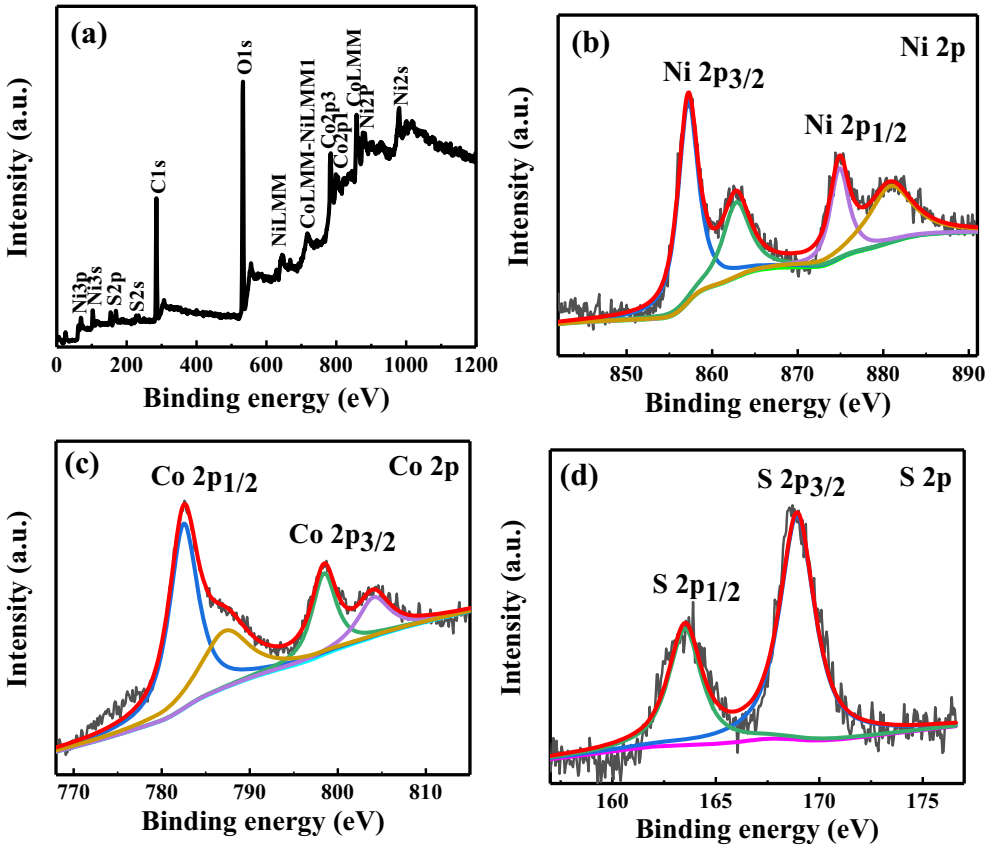

Figure 3. (a) XPS survey spectrum of $NiCo_2S_4$ sample; (b) high resolution spectrum of Ni 2p; (c) high resolution spectrum of Co 2p; (d) high resolution spectrum of S 2p.

Ni(II)/Ni(III) couple in the $NiCo_2S_4$ framework[31], which can be expressed with equation (4) as follows:

$$\mathrm{Ni(II)Co(III)_2S_4} + \mathrm{OH^-} \underset{\text{discharge}}{\overset{\text{charge}}{\longleftrightarrow}} \mathrm{Ni(III)Co(III)_2(OH)S_4} + e^- \quad (4)$$

This reaction equation is a little different from the one proposed earlier by Chen and Wan *et al* [32, 33] because it is considered to be more aligned with the fact observed in CV experiments, namely, only a pair of redox peaks from Ni(II)/Ni(III) couple occur, whereas the redox peaks from Co(III)/Co(IV) couple are not observed. Thus, the charge–discharge process is realized through the redox reaction of Ni(II)/Ni(III) couple.

Apparently, used as the electrode material for supercapacitors, $NiCo_2S_4$ can provide Faradaic pseudocapacitance via the redox reaction mentioned about. The specific capacitance of $NiCo_2S_4$ was estimated to

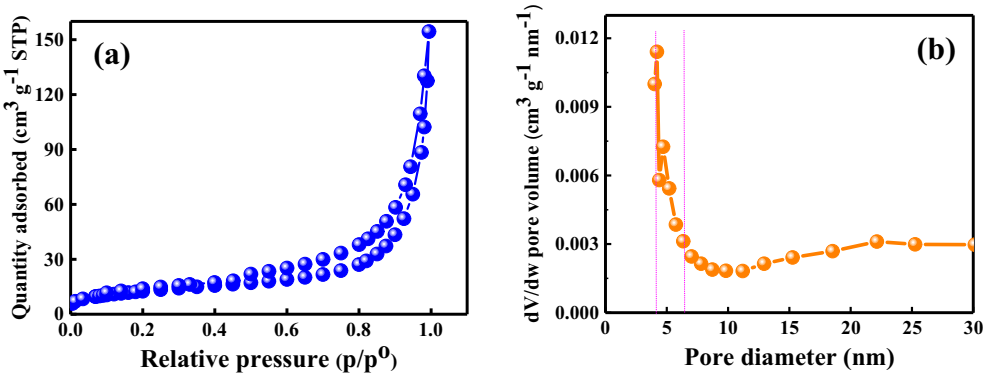

Figure 4. The N_2 adsorption-desorption isotherm (a) and pore size distribution (b) of the $NiCo_2S_4$ sample.

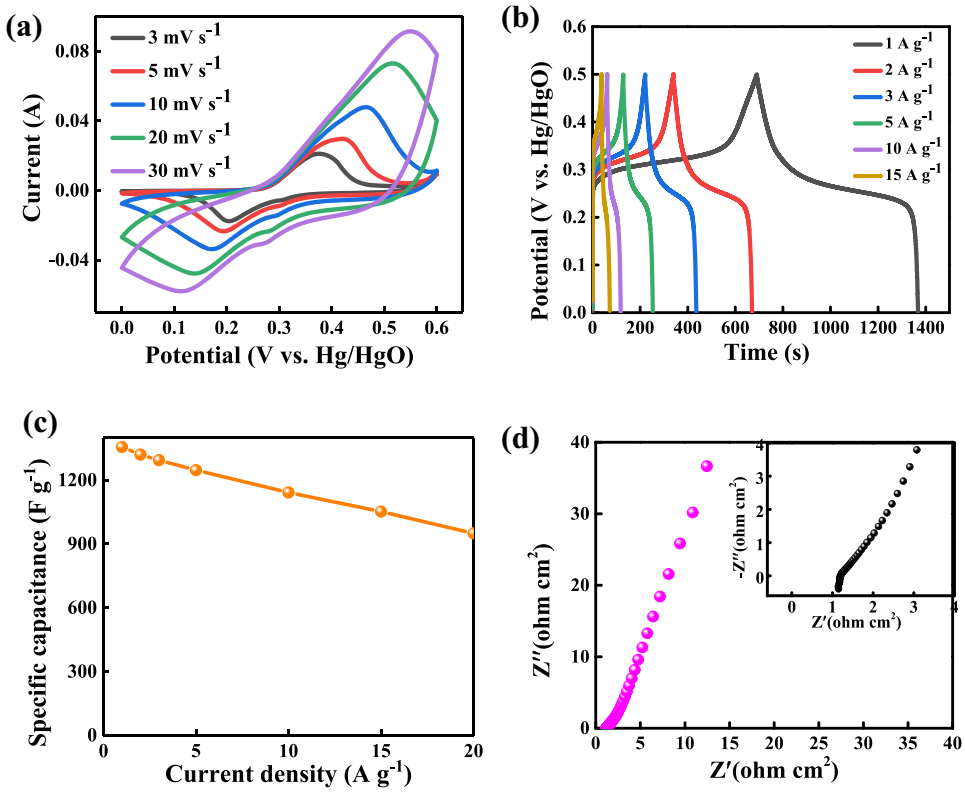

Figure 5. Electrochemical performances of the $NiCo_2S_4$ material: (a) CV curves at different scan rate; (b) GCD curves at different current densities; (c) The specific capacitance change as a function of current density; (d) Nyquist plot of the $NiCo_2S_4$ electrode.

be ca 1350 F g^{-1} at 1 A g^{-1} in terms of its galvanostatic charge–discharge curve in Figure 5(b). It should be noted that the specific capacitance value is related to the current density. As shown in Figure 5(c), the specific capacitance of $NiCo_2S_4$ decreases with increase of the current density from 1 to 20 A g^{-1}. When the current density increases to 20 A g^{-1}, the specific capacitance drops to 950 F g^{-1}, but still has ca 70% retention, presenting a relatively good rate capability. The galvanostatic charge–discharge curves possessing a potential plateaus shown in Figure 5(b) also confirm that $NiCo_2S_4$ belongs to battery-type material. For a battery-type electrode material, specific capacitance degradation with increase of the current density is inevitably prominent due to large electrochemical polarization resulting from a slow migration of electroactive species or the intercalation and de-intercalation of ions in a solid phase structure. This just is its defect compared to a capacitance-type electrode material because the latter only involves in electrolyte ions transport along the surface. Evidently, large electrochemical polarization will affect the rate capability and cyclic life of the battery-type electrode materials. The cyclic charge–discharge tests show that the $NiCo_2S_4$ with a ZIF-67 framework structure exhibits a poor cyclic stability. When the charge–discharge is less than 500 cycles, the specific capacitance has already presented a great attenuation (Figure 2S, Supplementary Information). This may be related to the instability of the material structure during charge–discharge process because it involves in intercalation and de-intercalation of OH^- ions in the crystal phase structure (equation 4). For materials immobilized on a solid electrode in a traditional way, such instability in architecture under action of electrochemical "pressure", e.g., agglomeration, sintering, dissolution, expansion and passivation, etc., is a universal phenomenon. This phenomenon may be related to the resistance of electron transfer or ions transport under an applied electric field. For instance, repeating intercalation and de-intercalation of OH^- ions in the crystal architecture of $NiCo_2S_4$ would cause inevitably a structural inflation and constriction, thus collapse of the structure[18].

In order to examine the resistance of electron transfer across interface and ions diffusion, EIS measurements were performed in the frequency range from 0.01 Hz to 100 kHz under the open-circuit

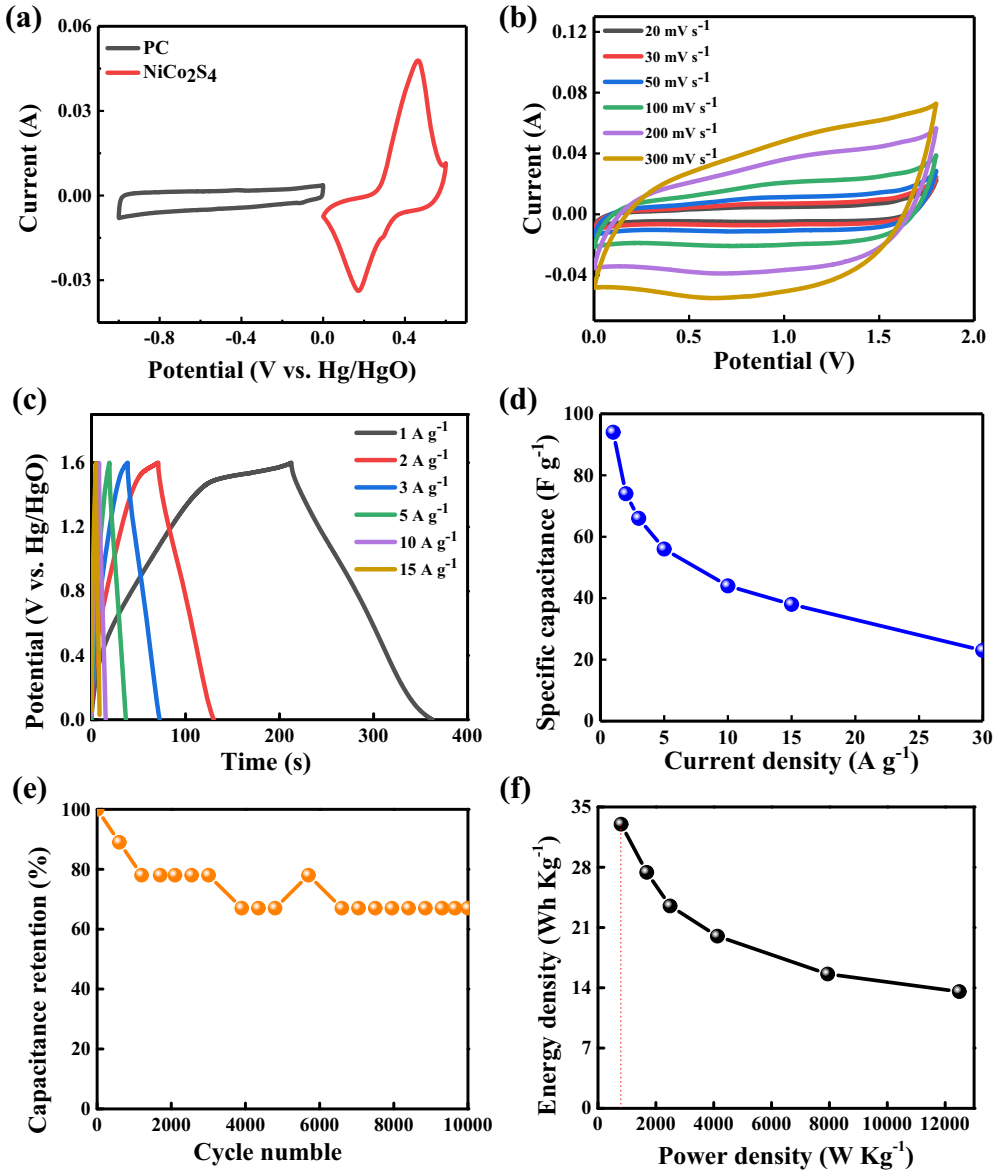

Figure 6. Electrochemical performances of the hybrid supercapacitor PC//$NiCo_2S_4$. (a) CV curves of $NiCo_2S_4$ and PC electrodes at a scan rate of 10 mV s^{-1}; (b) CV curves at different scan rate; (c) GCD curves at different current densities; (d) The specific capacitance change as a function of current density; (e) The cycling stability at the current density of 5 A g^{-1}; (f) Ragone plot.

potential and the AC amplitude of 5 mV, and the obtained Nyquist plot is illustrated in Figure 5(d). It can be seen that the high-frequency intersection of the Nyquist plot at the real axis gives a value of about 1.2 Ω, which is ascribed to the electrode resistance[34]. In the range of intermediate frequencies (corresponding to the interval of 1.2–2 Ω at the real axis), the Nyquist plot presents a nonvertical line with a medium slope, which is often used to describe diffusion layer resistance. Whereas in the range of low frequencies (corresponding to the interval of 2∼12 Ω at the real axis), the Warburg line[35] increase a little in slope but remains nonvertical versus the real axis, indicating that the charge–discharge process is limited by ion diffusion in the electrolyte[34]. Meanwhile, it also accounts for a small electron transfer resistance across interface between different materials, thus reflecting the capacitive feature of the $NiCo_2S_4$ electrode[36].

For practical application, the prepared $NiCo_2S_4$ was used as positive electrode material to assemble a hybrid supercapacitor device together with a self-prepared porous carbon (PC) as negative electrode material, expressed as PC//$NiCo_2S_4$. The measuring results in regard to the electrochemical performance of this device are presented in Figure 6. It can be seen from Figure 6(a), (b) that a potential window of 1.6 V

was obtained for the PC//$NiCo_2S_4$, much wider than that of the pristine $NiCo_2S_4$ or PC. Therefore, assembling of a hybrid supercapacitor can remarkably extend the device's operating voltage versus a symmetrical supercapacitor. Obviously, this is helpful to greatly enhancing device's energy density according to Eq. (2). The cyclic voltammograms in Figure 6(b) display the shape similar to rectangle, demonstrating that the main performance of PC//$NiCo_2S_4$ is capacitive behavior. This capacitance behavior primarily comes from the contribution of the negative electrode carbon material because the positive electrode active substance $NiCo_2S_4$ is battery-type electrode material. The specific capacitance of the PC//$NiCo_2S_4$, calculated from the discharge curves (Figure 6c), decreases from 94 to 23 F g^{-1} when the current density increases from 1 to 30 A g^{-1} (Figure 6d), presenting a poor rate capability. This phenomenon can be explained by the polarization effect of the $NiCo_2S_4$ positive electrode at large current density. Namely, during charge-discharge the rate of intercalation and de-intercalation of the OH^- ion in the $NiCo_2S_4$ crystal structure are slower than that of the electron transfer, leading to that the positive or negative charge is not compensated in time. As a result, the accumulated charge will hinder subsequent electron transfer, resulting in a rapid decrease in capacitance. With respect to the cyclic life, the specific capacitance drops to 67% of the original value when the charge-discharge at 5 A g^{-1} reached 10000 cycles (Figure 6e), displaying a good cyclic stability. Therefore, the cyclic stability for the PC//$NiCo_2S_4$ is much better than that for the pristine $NiCo_2S_4$ electrode material. The reason is not clear. We notice that in Figure 6(e), the capacitance retention ratio rises at the 4800 cycle number, then drops and remains stable again beyond the 6500 cycle number. This phenomenon may be ascribed to the activation of materials. Some deep layer $NiCo_2S_4$ active substances begin to react along with the permeation of electrolyte ions, thus leading to capacitance increase. However, electrochemical polarization and material's tiring make the capacitance decline again. Finally, multiple positive and negative factors together maintain the capacitance's stability.

Energy density (E) and power density (P) are usually another two critical parameters for estimating performance of an energy storage device. Generally, energy density varies with the power density. The curve that illustrates this change relationship is called as Ragone plot. The Ragone plot of PC//$NiCo_2S_4$ is shown in Figure 6(f). It can be seen that the energy density of PC//$NiCo_2S_4$ decreases with increase of the power density. A maximum energy density of about 33 Wh kg^{-1} at the power density of 800 W kg^{-1} was achieved under the experimental conditions. This value is higher than those of some other ASCs[37,38]. Such a high energy density results majorly from the contribution of the operating voltage of 1.6 V (Eq.2)[39].

4. Conclusions

A hollow cube $NiCo_2S_4$ nanomaterial was prepared via facile hydroxylation and sulfuration steps using the self-prepared ZIF-67 as a precursor. The as-prepared $NiCo_2S_4$ presents a specific capacitance high up to 1350 F g^{-1} at 1 A g^{-1} when used to be an electrode material for supercapacitor. For practical application, a hybrid supercapacitor PC//$NiCo_2S_4$ was assembled using $NiCo_2S_4$ as the positive electrode material and PC as the negative electrode material. The PC//$NiCo_2S_4$ device delivers an energy density of 33 Wh kg^{-1} at the power density of 800 W kg^{-1} and exhibits a good cyclic stability and a poor rate capability. Therefore, this kind of $NiCo_2S_4$ with a hollow cube nanostructure leaves much to be desired if used for a high performance supercapacitor.

Acknowledgments

This work is supported by the Key Science and Technology Planning Project of Hainan Province (Grant Number: ZDYF2018005; ZDYF2017083), the Innovative Research Project for Postgraduates of Hainan Province (Grant Number: Hyb2019-12), the Innovation and Entrepreneurship Projects for Chinese college students (Grant Number: Cxcyxj2018002; Hsyx-2018-24).

Supplementary Information (SI)

Figures 1S–3S are available at www.ias.ac/chemsci.

References

1. Miller J R and Simon P 2008 Electrochemical capacitors for energy management *Science* **321** 651
2. Huang P, Lethien C, Pinaud S, Brousse K, Laloo R, Turq V, Respaud M, Demortière A, Daffos B, Taberna P L, Chaudret B, Gogotsi Y and Simon P 2016 On-chip and freestanding elastic carbon films for micro-supercapacitors *Science* **351** 691
3. Li Y M, Han X, Yi T F, He Y B and Li X F 2019 Review and prospect of $NiCo_2O_4$-based composite materials for supercapacitor electrodes *J. Energy Chem.* **31** 54
4. Aricò A S, Bruce P, Scrosati B, Tarascon J M and Schalkwijk W V 2005 Nanostructured materials for

advanced energy conversion and storage devices *Nat. Mater.* **4** 366
5. Wang G, Zhang L and Zhang J 2012 A review of electrode materials for electrochemical supercapacitors *Chem. Soc. Rev*. **41** 797
6. Chen T, Shaoting Wei S T and Zhenghua Wang Z H 2020 $NiCo_2S_4$-Based Composite Materials for Supercapacitors *ChemPlusChem* **85** 43
7. Shinde S K, Ramesh S, Bathula C, Ghodake G S, Kim D Y, Jagadale A D, Kadam AA, Waghmode D P, Sreekanth T V M, Kim H S, Nagajyothi P C and Yadav H M 2019 Novel approach to synthesize $NiCo_2S_4$ composite for high performance supercapacitor application with different molar ratio of Ni and Co *Sci. Rep*. **9** 13717
8. Mohamed S G, Iftikhar Hussaina I and Shim J J 2018 One-step synthesis of hollow C-$NiCo_2S_4$ nanostructures for high-performance supercapacitor electrodes *Nanoscale* **10** 6620
9. Gogotsi Y and Simon P 2011 True performance metrics in electrochemical energy storage *Science* **334** 917
10. Ferris A, Garbarino S, Guay D and Pech D 2015 3D RuO_2 microsupercapacitors with remarkable areal energy *Adv. Mater*. **27** 6625
11. Wang C, Xu J, Yuen M-F, Zhang J, Li Y, Chen X and Zhang W 2014 Hierarchical composite electrodes of nickel oxide nanoflake 3D graphene for high-performance pseudocapacitors *Adv. Funct. Mater*. **24** 6372
12. Kurra N, Alhebshi N A and Alshareef H N 2014 Microfabricated pseudocapacitors using $Ni(OH)_2$ electrodes exhibit remarkable volumetric capacitance and energy density *Adv. Energy Mater*. **5** 1401303
13. Cakici M, Reddy K R and Fernando A M 2017 Advanced electrochemical energy storage supercapacitors based on the flexible carbon fiber fabric-coated with uniform coral-like MnO_2 structured electrodes *Chem. Eng. J*. **309** 151
14. Mani V, Govindasamy M, Chen S-M, Subramani B, Sathiyan A and Merlin J P 2017 Determination of folic acid using graphene/molybdenum disulfide nanosheets/-gold nanoparticles ternary composite *Int. J. Electrochem. Sci*. **12** 258
15. Govindasamy M, Mani V, Chen S-M, Sathiyan A, Merlin J P and Boopathy G 2016 polyaniline/nickel composite film modified electrode for sensitive electrochemical determination of ascorbic acid *Int. J. Electrochem. Sci.* **11** 10806
16. Lin Z, Goikolea E, Balducci A, Naoi K, Taberna P L, Salanne M, Yushin G and Simon P 2018 Materials for supercapacitors: When Li-ion battery power is not enough *Mater. Today* **21** 419
17. Yang Z H, Zhu X, Wang K, Ma G, Cheng H and Xu F F 2015 Preparation of $NiCo_2S_4$ flaky arrays on Ni foam as binder-free supercapacitor electrode *Appl. Surf. Sci*. **347** 690
18. Wang L L, Huang Y X, Li X S, Ma H, You C H, Liu J H, Huang Y Q, Hua Y J and Wang C T 2019 Preparation of urchin-like $NiCo_2O_4$ material and studies of its electrochemical performance for supercapacitors *Funct. Mater. Lett.* **12** 1950026
19. Lin L, Liu J, Liu T, Hao J, Ji K, Sun R, Zeng W and Wang Z 2015 Growth-controlled $NiCo_2S_4$ nanosheet arrays with self-decorated nanoneedles for high-performance pseudocapacitors *J. Mater. Chem*. **3** 17652
20. Xiao J, Wan L, Yang S, Xiao F and Wang S 2014 Design hierarchical electrodes with highly conductive $NiCo_2S_4$ nanotube arrays grown on carbon fiber paper for high-performance pseudocapacitors *Nano Lett.* **14** 831
21. Li Y, Cao L, Qiao L, Zhou M, Yang Y, Xiao P and Zhang Y 2014 Ni–Co sulfide nanowires on nickel foam with ultrahigh capacitance for asymmetric supercapacitors *J. Mater. Chem.* A **2** 6540
22. Xu X, Tian X, Li X, Yang T, He Y, Wang K, Song Y and Liu Z 2019 Structural and chemical synergistic effect of $NiCo_2S_4$ nanoparticles and carbon cloth for high performance binder-free asymmetric supercapacitors *Appl. Surf. Sci*. **465** 635
23. Chen W, Xia C and Alshareef H N 2014 One-Step electrodeposited Nickel Cobalt Sulfide nanosheet arrays for high-performance asymmetric supercapacitors *ASC Nano* **8** 9531
24. Chen H, Jiang J, Zhang L, Xia D, Zhao Y, Guo D, Qi T and Wan H 2013 In situ growth of $NiCo_2S_4$ nanotube arrays on Ni foam for supercapacitors: maximizing utilization efficiency at high mass loading to achieve ultrahigh areal pseudocapacitance *J. Power Sour.* **254** 249
25. Hu H, Guan B Y and Lou X W 2016 Construction of complex CoS hollow structures with enhanced electrochemical properties for hybrid supercapacitors *Chem* **1** 102
26. Hu H, Guan B, Xia B and Lou X M 2015 Designed formation of Co_3O_4/$NiCo_2O_4$ double-shelled nanocages with enhanced pseudocapacitive and electrocatalytic properties *J. Am. Chem. Soc*. **137** 5590
27. Jiang Z, Li Z, Qin Z, Sun H, Jiao X and Chen D 2013 LDH nanocages synthesized with MOF templates and their high performance as supercapacitors *Nanoscale* **5** 11770
28. Wu R, Wang D P, Rui X, Liu B, Zhou K, Law A W K, Yan Q, Wei J and Chen Z 2015 In situ formation of hollow hybrids composed of cobalt sulfides embedded within porous carbon polyhedra/carbon nanotubes for high performance lithium ion batteries *Adv. Mater.* **27** 3038
29. Fan G, Li F, Evans D G and Duan X 2015 Catalytic applications of layered double hydroxides: recent advances and perspectives *Chem. Soc. Rev*. **45** 7040
30. Wang Y, Song Y and Xia Y 2016 Electrochemical capacitors: mechanism, materials, systems, characterization and applications *Chem. Soc. Rev*. **45** 5925
31. Brousse T, Bélanger D and Long J W 2015 To be or not to be pseudocapacitive *J. Electrochem. Soc*. **162** A5185
32. Chen C-Y, Shih Z-Y, Yang Z and Chang H-T 2012 Carbon nanotubes/cobalt sulfide composites as potential high-rate and high-efficiency supercapacitors *J. Power Sources* **215** 43
33. Wan H, Jiang J, Yu J, Xu K, Miao L, Zhang L, Chen H and Ruan Y 2013 $NiCo_2S_4$ porous nanotubes synthesis via sacrificial templates: high-performance electrode materials of supercapacitors *CrystEngComm* **15** 7649
34. Mei B A, Munteshari O, Lau J, Dunn B and Pilon L 2018 Physical Interpretations of Nyquist Plots for

EDLC Electrodes and Devices *J. Phys. Chem. C* **122** 194
35. Bard A J, Faulkner L R, Leddy J and Zoski C G 1980 *Electrochemical Methods: Fundamentals and Applications* (Hoboken: Wiley) vol. 2
36. Stoller M D, Park S, Zhu Y, An J and Roff R S 2008 Graphene-based ultracapacitors *Nano Lett.* **8** 3498
37. Hou L H, Bao R, Chen Z, Rehan M, Tong L, Pang G and Yuan C 2016 Comparative investigation of hollow mesoporous $NiCo_2S_4$ ellipsoids with enhanced pseudocapacitances towards high-performance asymmetric supercapacitors *Electrochim. Acta* **214** 76
38. Cao L, Tang G, Mei J and Liu H 2017 Construct hierarchical electrode with $Ni_xCo_{3-x}S_4$ nanosheet coated on $NiCo_2O_4$ nanowire arrays grown on carbon fiber paper for high-performance asymmetric supercapacitors *J. Power Sources* **359** 262
39. Li Z, Xin Y, Jia H, Wang Z, Sun J and Zhou Q 2017 Rational design of coaxial MWCNT-COOH@$NiCo_2S_4$ hybrid for supercapacitors *J. Mater. Sci*. **52** 9661